Fabrication and Test of C3a: A Six-Layer Subscale Canted $\cos\theta$ Dipole Magnet Using High-Temperature Superconducting CORC Wires

Dmytro Abraimov, *Member, IEEE*, Diego Arbelaez, Lucas Brouwer, Helen Feng, Paolo Ferracin, *Senior Member, IEEE*, William B. Ghiorso, Hugh C. Higley, Mariusz Juchno, Andy Lin, Thomas Lipton, Linqing Luo, *Member, IEEE*, Maxim Marchevsky, Ian Pong, *Senior Member, IEEE*, Soren O. Prestemon, Kyle Radcliff, José Luis Rudeiros Fernández, *Member, IEEE*, Anjana Saravanan, Tengming Shen, *Senior Member, IEEE*, Reed Teyber, Marcos Turqueti, *Senior Member, IEEE*, Danko van der Laan, *Senior Member, IEEE*, Xiaorong Wang, *Senior Member, IEEE*, Jeremy D. Weiss, *Member, IEEE*, and Yuxin Wu

***Abstract*—REBCO coated conductors have a strong potential for high-field magnet applications. The REBCO technology, however, is still in its infancy for accelerator magnet applications. As part of the U.S. Magnet Development Program, we developed a six-layer canted $\cos\theta$ dipole magnet, C3a, using CORC wires developed by Advanced Conductor Technologies LLC. All the layers were wound using a semiautomated winding machine. Three layers of the magnet used CORC wires containing the SuperPower "AP" REBCO tapes and the remaining layers used the wires containing the "HM" tapes. At 77 K, both kinds of CORC wires showed 5% to 10% degradation, after bending to a minimum bend radius of 30 or 35 mm, with respect to the self-field critical current measured before winding. At 4.2 K, the magnet reached 9.5 kA at a ramp rate of 9 A s^{-1} and generated a dipole field of 1.4 T. The critical current of one layer degraded by 4% after a current transient up to 10.5 kA ramped in an averaged rate of 175 kA s^{-1} or 20 T s^{-1}. We confirmed the HM CORC wire can carry a higher current than the AP CORC wire at 4.2 K. The test results of the C3a magnet showed that the fabrication and assembly procedure can be used for the upcoming full-scale C3 magnet.**

***Index Terms*—REBCO, CORC wire, dipole magnet.**

Received 23 November 2024; revised 23 March 2025 and 21 April 2025; accepted 21 April 2025. Date of publication 28 April 2025; date of current version 20 May 2025. This work was supported in part by the U.S. Magnet Development Program (MDP) through Director, Office of Science, Office of High Energy Physics of the US Department of Energy under Contract DEAC02-05CH11231. *(Corresponding author: Xiaorong Wang.)*

Dmytro Abraimov is with the Applied Superconductivity Center, National High Magnetic Field Laboratory, Florida State University, Tallahassee, FL 32310 USA.

Diego Arbelaez, Lucas Brouwer, Helen Feng, Paolo Ferracin, William B. Ghiorso, Hugh C. Higley, Mariusz Juchno, Andy Lin, Thomas Lipton, Linqing Luo, Maxim Marchevsky, Ian Pong, Soren O. Prestemon, José Luis Rudeiros Fernández, Anjana Saravanan, Tengming Shen, Reed Teyber, Marcos Turqueti, Xiaorong Wang, and Yuxin Wu are with Lawrence Berkeley National Laboratory, Berkeley, CA 94720 USA (e-mail: XRWang@lbl.gov).

Kyle Radcliff, Danko van der Laan, and Jeremy D. Weiss are with Advanced Conductor Technologies (ACT), Boulder, CO 80301 USA, and also with the University of Colorado, Boulder, CO 80309 USA.

Color versions of one or more figures in this article are available at https://doi.org/10.1109/TASC.2025.3565222.

Digital Object Identifier 10.1109/TASC.2025.3565222

I. Introduction

HIGH-TEMPERATURE superconductors, such as $REBa_2Cu_3O_{7-x}$ (REBCO, RE = rare earth) are expected to enable a dipole field above 20 T. Such a dipole field can allow future circular accelerators to collide particles at unprecedented energy levels. However, the REBCO conductor and magnet technology needs to be significantly advanced before we can leverage the full potential of REBCO conductors. Besides the demanding requirements on magnet performance and protection [1], [2], [3], a key issue is how to realize dipole magnets given a certain REBCO cable architecture.

The EuCARD and EuCARD2 programs led the development of REBCO accelerator magnets, generating the record dipole fields of 5.4 T in a racetrack coil using essentially a stack of four REBCO tapes [4] and 4.5 T in a 40-mm aperture of a magnet using Roebel cables [5], both at liquid helium temperature around 4.5 K. More details can be found in a review article by Rossi and Senatore [6].

The U.S. Magnet Development Program (MDP), sponsored by the DOE Office of High Energy Physics, is developing REBCO magnet technology with a focus on round wires, such as CORC[1] and STAR[1] wires [7], [8]. Round wires using REBCO tapes are electromagnetically and mechanically isotropic [9], [10], [11], [12], [13]. They are expected to be convenient for magnet design, analysis, and fabrication, which motivates the magnet development using round REBCO wires. Various magnet designs are being studied, including conductor on molded barrel [14], common coil [15] and canted $\cos\theta$ (CCT) [16], [17]. A new design called "Unilayer" was proposed recently [18].

In addition to the effort at the MDP, several other institutes are also developing magnets using round REBCO conductors for particle accelerator applications [19], [20], [21], [22], [23].

The future CCT magnet using CORC wires, C3, aims at a dipole field of 5 T at 4.2 K. Compared to the earlier CORC CCT magnets, the C3 magnet will use the CORC wire based on the

[1]Registered trademark.

TABLE I
MAIN PARAMETERS FOR THE C3A MAGNET

Design parameters	Unit	Layer 1	2	3	4	5	6	7, shell
Inner diameter (ID)	mm	65.0	85.2	99.4	113.6	127.8	142.0	156.2
Wire center diameter	mm	78.1	92.3	106.5	120.7	134.9	149.1	
Outer diameter (OD) at mandrel ends	mm	84.1	98.3	112.5	126.7	140.9	155.1	207.0
Spar thickness	mm	4.5	1.5	1.5	1.5	1.5	1.5	
Wire turns		3						
Wire length	m	2.3	2.6	2.9	3.3	3.7	4.0	
Groove diameter	mm	4.1						
Wire tilt angle at the mid-plane	degree	50	−50	−35	35	27	−27	
Minimum bending radius of the wire center line	mm	30	35	30	35	30	35	
Nominal layer length	mm	708						
Layer material		aluminum bronze 954						aluminum 6061-T6
Measured gap between wires at the mid-plane	mm	0.29	0.28	0.32	0.37	0.58	0.60	
Layer weight including conductors	kg	12.0	10.2	11.8	13.3	14.9	16.5	27.7

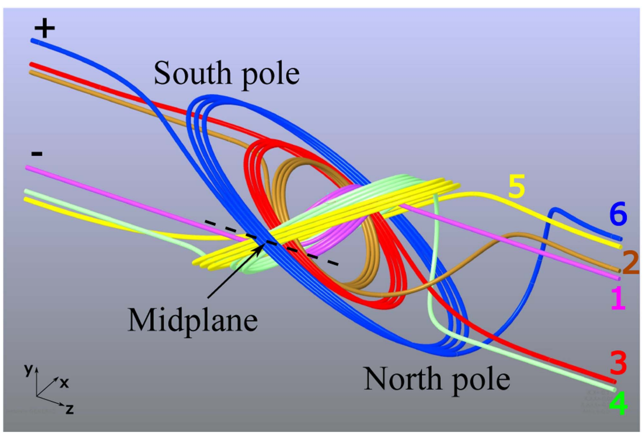

Fig. 1. Layout of the six layers for the C3a magnet. Each layer is numbered. Magnet current flows from Layers 6 to 1. The dashed line indicates one midplane of the magnet.

high-magnetic (HM) field REBCO tape developed by SuperPower Inc. for low-temperature high-field applications. Each batch of the HM tapes should have a minimum critical current of 350 A at 4.2 K, 6 T. The magnet will have six nested layers with full-depth radial grooves, which requires a new winding procedure.

To address these new requirements and to reduce the fabrication risk of the C3 magnet, we made a subscale magnet C3a. The C3a magnet has the same nominal design as C3, except for only three turns of conductors in each layer of the magnet. By making and testing C3a, we intended to address the following questions.

1) How to make and assemble the coils into a magnet?
2) What is the bending and transport performance of the HM CORC wire?
3) What is the magnet performance?
4) What is the performance of the electrical joints?
5) How to install optical fiber into the coil? Does the fiber offer any insight into the magnet behavior?

Here, we address the first four questions. The last question is addressed in a companion paper [24]. We used a new winding machine to wind all the coils. We developed a procedure to fill the Stycast into the radial gaps between the coils. We also confirmed that the HM CORC wires carried a higher current than the AP wires at 4.2 K. The new electrical terminations yielded joint resistances comparable to the previous joints at 4.2 K. The fabrication and test of C3a set the stage to fabricate and test the C3 magnet toward a dipole field of 5 T.

II. MAIN PARAMETERS OF THE MAGNET AND CONDUCTOR

The C3a magnet has six nested layers; each layer has three periodic turns of CORC wires (Fig. 1). Each layer is an individual coil. Here, "layer" and "coil" are used interchangeably. When the layout is projected to the y-z plane, the angle between the periodic turns and the z-axis give the tilt angle of each layer (Table I). When projected to the x-y plane, the center of the wire becomes a circle. The wire center diameter in Table I refers to the diameter of such a circle.

The C3a magnet used two types of CORC wires. One type used the advanced pinning (AP) REBCO tapes and the other used the HM tapes. The HM tapes are developed to carry more current at low temperatures and in background magnetic fields, though their performance tends to be lower at temperatures above 30 K, compared to the AP tapes. SuperPower Inc. produced both kinds of commercial REBCO tapes [25].

The Applied Superconductivity Center at Florida State University measured the critical current of tape samples [26], [27]. ACT used the data to allocate tapes for the CORC wire fabrication. Fig. 2 shows the measured critical current of sample AP and HM tapes. The samples represent the tape batches that constituted 90% of the tapes used in each type of the CORC wires reported here.

Table II lists the main parameters of the CORC wires used in C3a.

We intended to use only the HM CORC wire in the C3a magnet for early feedback on the wire performance. The tape production, however, had challenges and took longer than expected. We used the AP CORC wire that was readily available for some of the layers to minimize the delay of the magnet fabrication. Table III shows the type of wire used in each layer.

III. MAGNET FABRICATION AND ASSEMBLY

A. Mandrel Fabrication

Like the other CCT magnets developed at LBNL [28], [29], [30], [31], we used cylinders of aluminum bronze 954 alloy

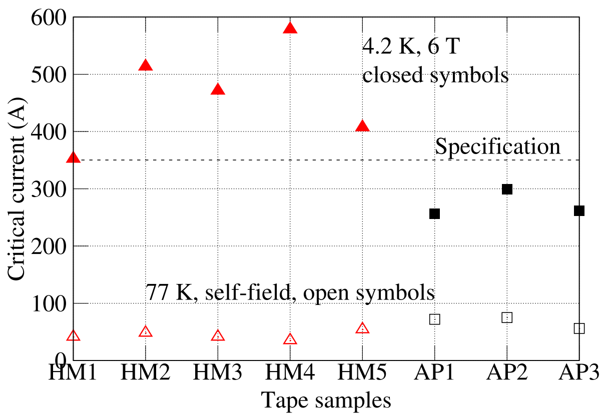

Fig. 2. Critical current of the 2 mm wide tape samples used in the HM- and AP-CORC wires. Open symbols: 77 K, self-field. Closed symbols: 4.2 K, 6 T, with the field perpendicular to the tape broad surface. The dashed line indicates the critical-current specification at 4.2 K and 6 T for the HM tape order.

TABLE II
MAIN PARAMETERS OF THE CORC WIRES USED IN THE C3A MAGNET

Parameter	Unit	AP	HM
Tape vendor		SuperPower Inc.	
Number of tapes		30	
Layers of tapes		12	
Tapes per layer		2 to 3	
Tape width	mm	2	
Substrate thickness	μm	30	
Cu thickness per tape side	μm	5	
Average tape I_c	A	67	44
Estimated wire I_c	kA	1.4 to 1.6	0.9 to 1.0
Fabricated wire length	m	26	10
Polyester jacket thickness	μm	30	
Nominal wire diameter	mm	3.75	3.73
Cu core diameter	mm	2.54	
Cu to non-Cu ratio		1.0	

The critical current is at 77 K, self-field.

TABLE III
CRITICAL CURRENT AND n VALUE OF THE CORC WIRE IN EACH LAYER AT 77 K, SELF-FIELD, DETERMINED AT 20 μV CRITERION ACCORDING TO (1)

Layer	Conductor	$R_{\min}$ (mm)	Before winding I_c (A)	Before winding n (-)	After winding I_c (A)	After winding n (-)	After Stycast I_c (A)	After Stycast n (-)
1	AP	30	1,460	8.0	1,145	7.7	1,103	7.2
2	AP	35	1,588	19.1	1,250	24.0	1,035	17.8
3	AP	30	1,550	20.4	1,268	24.9	1,245	22.9
4	AP	35	1,379	10.7	1,124	13.2	1,057	12.0
6	AP	35	-	-	1,121	17.1	1,089	15.7
1b	HM	30	-	-	654	27.0	635	24.2
2b	HM	35	908	30.7	660	28.4	652	27.0
5	HM	30	899	28.5	649	27.0	643	23.0

$R_{\min}$ denotes the minimum bend radius of the longitudinal axis of the CORC® wire in each layer.

as the mandrel material for the C3a magnet. A four-axis CNC machine cut grooves with a round bottom. We call it a radial groove because its opening is normal to the cylindrical surface of the mandrels. Unlike the half-depth radial groove used in the C2 magnet, C3a mandrels had a full depth and the CORC wire was below the outer surface of the mandrel after winding.

We minimized the gap between the neighboring wires in the coil midplane (Fig. 1). Although it increased the efficiency in generating the dipole field [32], the metal ribs became too thin, < 0.5 mm, to machine. We therefore removed the ribs in the coil

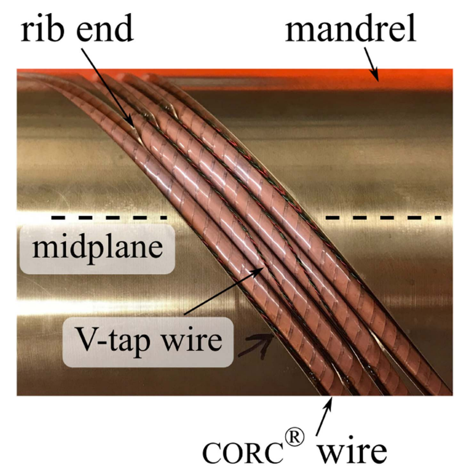

Fig. 3. Closeup view of three turns of CORC wires of Layer 1b. The voltage-tap wire crosses from one side to the other side of the CORC wire at the coil midplane indicated by the dashed line.

midplane completely. The ribs appeared when they were about 1-mm thick (Fig. 3).

The nominal radial clearance between the neighboring mandrels increased from 90 μm in C2 [31] to 575 μm in C3a (Table I). The bigger clearance facilitated the assembly of the layers and allowed Stycast 2850 MT epoxy to fill the radial gap between the layers.

Before winding, we used silicon carbide polishers (Dedeco 4592, grit size 120) to polish the grooves in each mandrel to remove the sharp edges.

B. Electrical Termination

The electrical terminations for the CORC wire consisted of a 203-mm long Cu tube filled with indium. The oxygen-free high-conductivity Cu tube had an outer diameter of 7.94 mm and an inner diameter of 6.31 mm. We trimmed the REBCO tapes inside the Cu tube to maximize the exposure of every tape to the solder, following the established procedure [33], [34].

We developed a new method to fill molten indium into the Cu tube. The Cu tube had an array of holes [Fig. 4(a)]. With both ends of the Cu tube sealed by an aluminum foil, molten indium filled the Cu tube through the holes [35]. Previously, the CORC wire was positioned vertically when filling molten indium [31]. With the new method, we can install the termination with the CORC wire positioned horizontally, convenient for handling a heavy coil [Fig. 4(b)].

The termination was then clamped into Cu adapters with indium foils [31]. Cu adapters with two parallel grooves were used to connect the CORC terminations from the neighboring layers, forming the interlayer joints (Fig. 7).

C. Coil Winding and Fabrication

When winding the previous C2 magnet, we realized that a new winding method was necessary for mandrels with a full-depth radial groove [31]. Inspired by a CCT winding machine developed by G. Kirby at CERN [36], we made Winder Mark 2 that moved the mandrel in three axes, positioning the groove

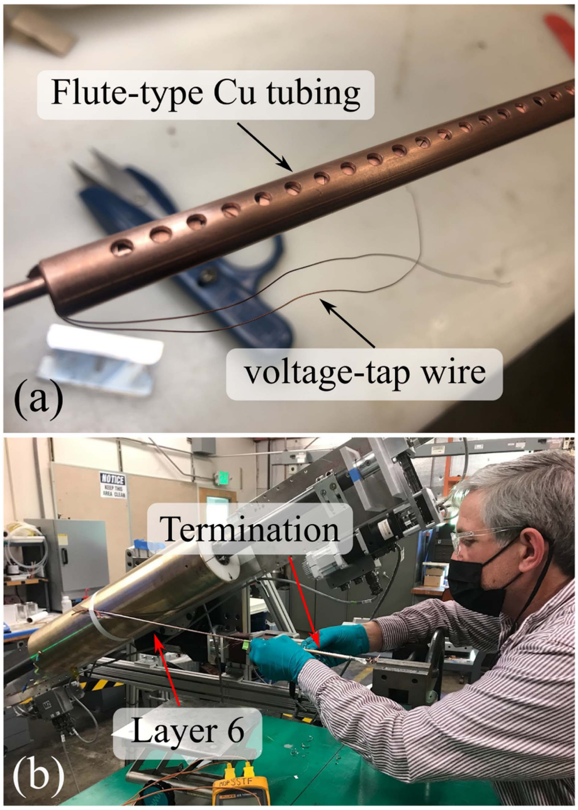

Fig. 4. (a) Cu tube as part of the electrical termination of CORC wire. (b) H. Higley installing the termination for Layer 6, near the end of winding.

Fig. 5. W. Ghiorso setting up Winder Mark 2.

to accommodate the incoming wire from the source spool. The source spool was a few meters away from the mandrel. The winder took the coordinates of center line of the groove as the input to determine the motion of the mandrel. Fig. 5 shows the winder. Several other groups also developed automated machines to wind magnets using REBCO tapes [37], [38].

Before winding, the conductor with the terminations was wound to a source spool of an outer diameter of 364 mm. All the layers were wound with a tension of about 25 N on the CORC wire. A few temporary or permanent electrical shorts occurred

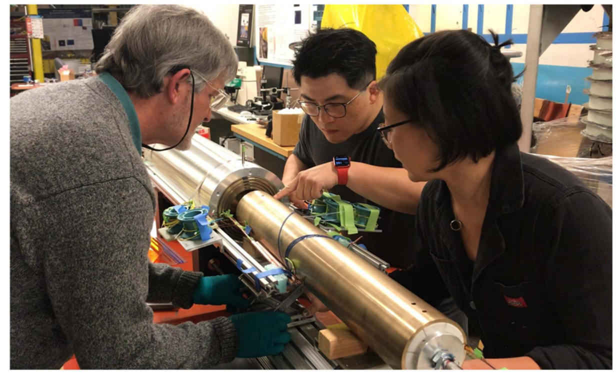

Fig. 6. H. Higley (left), A. Lin (center) and H. Feng (right) inserting Layer 2b into Layer 3. Spools of optical fibers were secured at the lead end of the assembled layers.

between the CORC wire and mandrel when the edge of the groove damaged the polyester jacket of the CORC wire.

We co-wound optical fibers along the CORC wire after the coil winding [24]. A triplet of solid Cu instrumentation wires (MWS Twistite) was then co-wound along the CORC wire for the layer-voltage measurement (Section IV).

In some layers, the triplet crossed from one side of the CORC wire to the other side at the coil midplane because it helped stabilize the triplet under tension (Fig. 3). The crossing facilitated the triplet winding but led to a stronger inductive component in the voltage signal across the layer.

The CORC wire in the long straight exits in Layers 1b and 2b (Fig. 1) tended to come out of the groove. Winding tension cannot keep the wire in the groove. We used short round rubber pieces to press and hold the wire inside the groove until we applied the Stycast.

We also co-wound an acoustic waveguide along the CORC wire in Layer 2 for a distributed sensing of local temperature rise [39]. The results will be reported elsewhere.

The final step of the coil fabrication was to fill the groove with Stycast 2850 MT. The cured epoxy can constrain and support the CORC wires against the electromagnetic forces. We first applied a water-based mold release to the outer surface of the mandrel, except for the regions with the CORC wire. Lack of a vacuum-pressure impregnation technique, we painted the Stycast, mixed with Catalyst 23LV, on top of the CORC wire. We wrapped the mandrel using a release-coated polyester tape (Fibre Glast 1791), with a 50% overlap, during painting to contain the wet Stycast. We removed the tape and residual epoxy on the mandrel surface after the epoxy cured overnight.

D. *Magnet Assembly*

We assembled the magnet by manually sliding the inner layers into the outer layers, starting from Layer 6 into the aluminum shell (Fig. 6). The return end of the inner layer entered the outer layer first because the optic fiber at the return end was short and easier to manage.

Once a layer was inserted, we shimmed and centered the mandrel layers using stainless-steel pins and thin Kapton shims. The stainless-steel pins were inserted into the alignment holes at

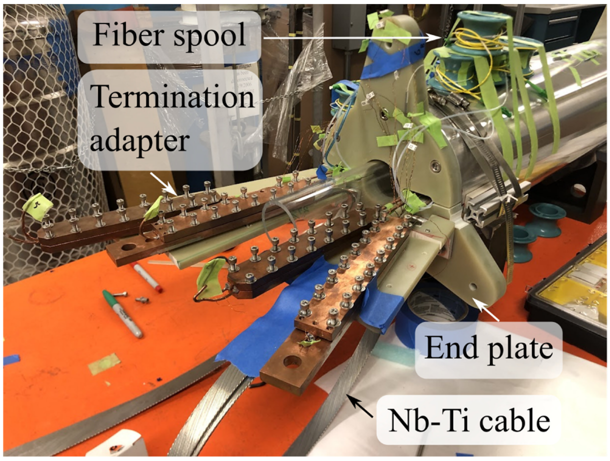

Fig. 7. Lead end of the C3a magnet during the assembly. Counting from left to right, the first and third Cu block assemblies were for inter-layer joints; the second Cu block was for the negative lead from Layer 1b and the fourth block was for the positive lead from Layer 6.

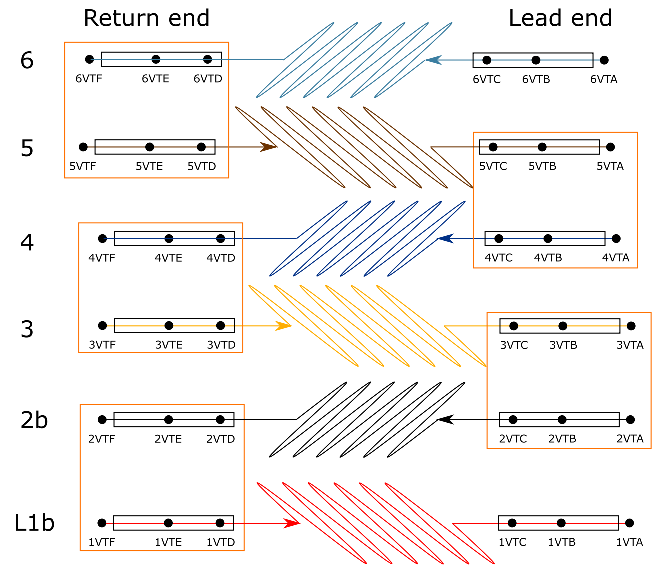

Fig. 8. Voltage tap configuration for the C3a magnet. The black boxes are terminations. The orange boxes indicate the inter-layer joints. Current flows from Layers 6 to 1, as indicated by the arrows.

both ends of the mandrels to align the layers longitudinally and azimuthally. Three Kapton shims at each end of the mandrels were roughly 120° apart. The thicknesses of the shims were within ± 100 μm of the nominal radial gap of 575 μm.

When the assembly was completed, we replaced the pins with a new set, each consisting of a stainless-steel pin with a G10 jacket to prevent the pins from electrically shorting the mandrels [31].

We filled the radial gaps between the neighboring layers using Stycast 2850 MT as a practice to mechanically couple all the layers against the electromagnetic forces (Appendix A).

After the epoxy cured, we attached a G10 plate to the aluminum shell at both ends of the magnet. The triangular G10 plates supported the Cu adapters for the electrical joints (Fig. 7) and helped position the magnet inside the cryostat.

We measured the electrical resistance between the conductor and the mandrel for each layer before installing the Cu termination adapters. Layer 1b had 3 Ω between the conductor and mandrel; the other five layers had more than 60 MΩ. The neighboring layers were found to be electrically isolated.

A stack of two Nb-Ti Rutherford cables were soldered to the back of the Cu termination adapters as part of the current leads (Fig. 7). Each cable, with 34 strands, can carry 17 kA at 5 K, 5 T [40], [41], enough to test the C3a magnet at 4.2 K.

IV. Measurement Setup and Protocol

We measured three voltage signals across each layer (Fig. 8). They are V_2 between taps C and D, each tap about 5 mm within the end of the termination; V_1 between B and E that were at the center of the termination; and V_0 between A and F that were soldered to the Cu core outside the termination. We used the V_2 data to report the magnet performance.

To monitor the magnet temperature, we used a calibrated Cernox sensor mounted next to the lead-end joints and a platinum thermometer (PT-103) touching the bottom of the cryostat. They also provided some redundancy to the level sensors.

The dipole field at the center of the magnet aperture was measured using a calibrated cryogenic Hall sensor (F. W. Bell BHA-921).

National Instruments (NI) 9238 modules were used to digitize the magnet current, the layer voltage, and the Hall sensor voltage, at a sampling rate of 1.6 kHz. The V_2 voltage signals were also measured with Keithley 2182A multimeters at a rate of 1Hz. The magnet current, interlayer joint voltages, the Hall probe voltage, and the voltages across the Nb-Ti current leads and vapor-cooled leads were also measured by a Keithley 2010 multimeters with an internal scanner card.

During the coil fabrication, we measured the critical current of the CORC wire at 77 K at three steps: 1) before winding; 2) after winding; and 3) after applying Stycast (Appendix B). We skipped the measurement before winding for Layers 1b and 6 to practice the procedure for the upcoming C3 magnet where the lead-end termination will be installed before completing the coil winding.

The magnet was tested twice at 77 K with a warmup to room temperature between the tests. The magnet was tested at 4.2 K following the second 77 K test, without warming up to room temperature. We did not connect the C3a magnet to any external energy-extraction resistor.

V. Results and Discussions

A. Critical-Current Retention of the CORC Wires At Different Steps of Coil Fabrication, 77 K

Fig. 9 shows the $V_2(I)$ for Layer 2 using the AP CORC wire and Layer 2b using the HM wire.

We used the following power-law fit to characterize the measured $V(I)$ data

$$V = V_{\text{offset}} + IR + V_c \left(\frac{I}{I_c}\right)^n \tag{1}$$

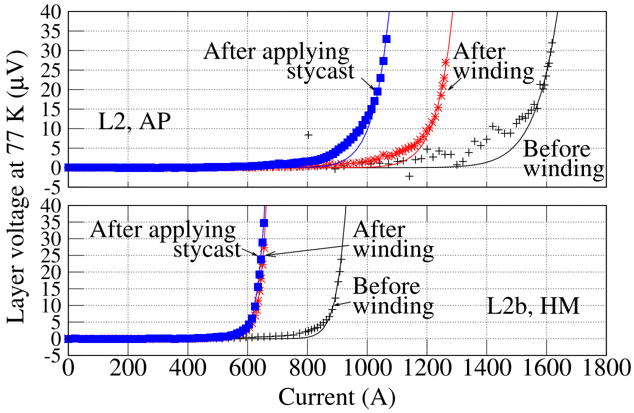

Fig. 9. $V_2(I)$, in symbols, for the CORC wire, before and after winding, and after applying Stycast. Top: Layer 2 using the AP wire. Bottom: Layer 2b using the HM wire. 77 K, self-field. The lines are power-law fits according to (1).

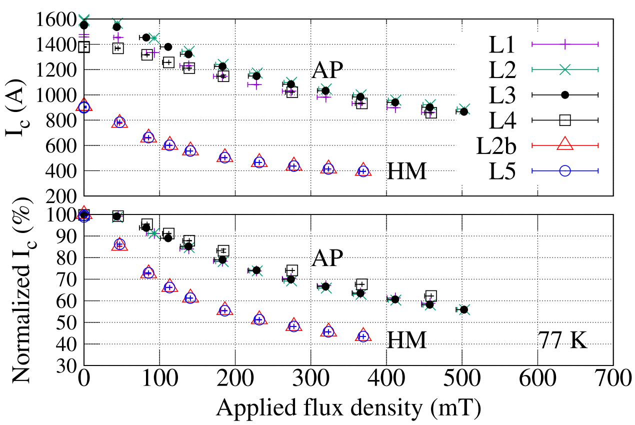

Fig. 10. Top: I_c of the CORC wires used in several layers of C3a as a function of applied flux density transverse to the longitudinal axis of the wire. The x errorbars indicate the uncertainty of the applied flux density. The y errorbars indicate the range of the measured I_c of the wire. Bottom: I_c of the CORC wires normalized to the their self-field values. Before winding, 77 K.

where V_{offset} is the voltage offset and R is the resistance between the voltage taps, usually associated with the termination resistance when the voltage taps are inside the electrical terminations. We removed the voltage due to offset and termination resistance in the $V(I)$ plots unless otherwise stated. The critical current I_c is defined at a voltage criterion, V_c, of 20 μV, corresponding to an electric field of 9 μV m^{-1} for Layer 1 and 5 μV m^{-1} for Layer 6.

Fig. 10 shows the I_c of the CORC wires, before winding, as a function of the applied transverse flux density. The similar transport performance measured from the HM CORC wires used for Layers 2b and 5 suggested a uniform critical current over at least a 6-m long HM CORC wire. Fig. 11 shows the n value of the CORC wires.

Table III gives the evolution of the I_c and n value of the CORC wire in each layer at each step of the coil fabrication.

Table IV lists the I_c normalized to that before winding. The I_c of Layer 4, before winding, was used for Layer 6. The I_c of Layer 5, before winding, was used for Layer 1b. Column

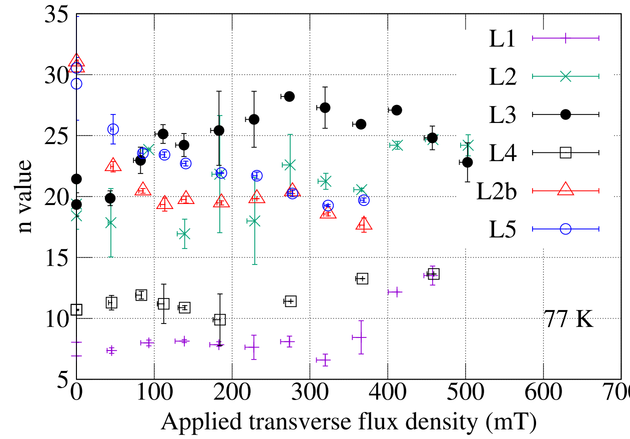

Fig. 11. n value of the CORC wires as a function of applied flux density transverse to the longitudinal axis of the wire. The x errorbars indicate the uncertainty of the applied flux density. The y errorbars indicate the range of the measured n value. The red triangles and blue open circles represent the data for the HM CORC wires. Before winding, 77 K.

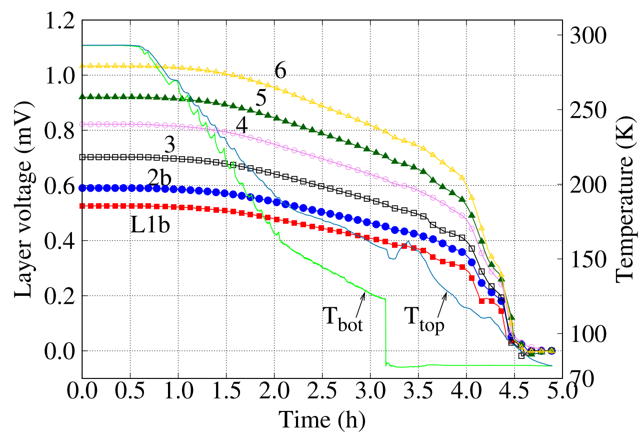

Fig. 12. Voltage across each layer of C3a at 100 mA during the cooldown from room temperature to 77 K. Secondary y-axis: temperature readings.

"Self-field effect only" in Table IV gives the normalized I_c as expected from the increased self-field after winding. Column "Difference" is the difference between values after winding and the estimated value considering only the self-field effect.

Painting Stycast caused 2% or less reduction in the I_c for all the layers except for Layers 2 and 4. The 2% reduction was consistent with the C2 experience [31]. Layer 2 showed an excessive 14% degradation and was replaced with Layer 2b (Fig. 9 and Table IV). We suspected that, during the test preparation of Layer 2, the flexing single G10 boards supporting the current leads were accidentally strained and degraded the CORC wire outside the mandrel. We strengthened the G10 board by adding 80/20 aluminum rails for later coils.

B. Magnet Behavior At 77 K

Fig. 12 shows the voltage across each layer during the cooldown of the C3a magnet from room temperature to 77 K with a 100-mA current. All the layers became superconducting almost simultaneously.

TABLE IV
CRITICAL CURRENT OF THE CORC WIRE IN EACH LAYER AT 77 K, SELF-FIELD, NORMALIZED TO THE VALUE BEFORE WINDING IN TABLE III

Layer	Conductor	$R_{\min}$ (mm)	After winding	After Stycast	Self-field effect only	Difference	Used in C3a
1	AP	30	78%	76%	86%	−8%	No
2	AP	35	79%	65%	86%	−7%	No
3	AP	30	82%	80%	87%	−5%	Yes
4	AP	35	82%	77%	91%	−9%	Yes
6	AP	35	81%	79%	92%	−11%	Yes
1b	HM	30	73%	71%	80%	−7%	Yes
2b	HM	35	73%	72%	78%	−5%	Yes
5	HM	30	72%	71%	81%	−9%	Yes

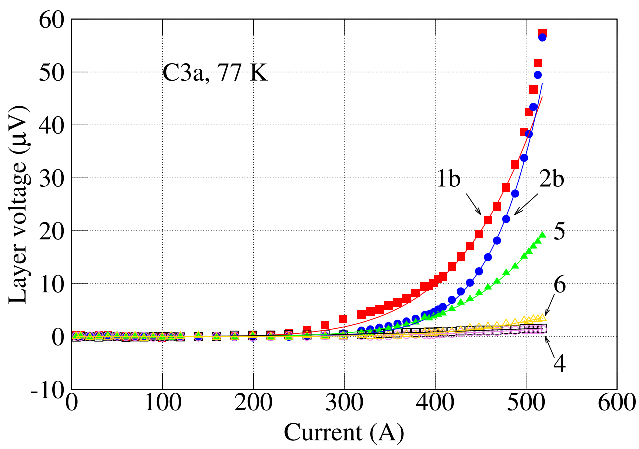

Fig. 13. $V_2(I)$ across each layer of the C3a magnet at 77 K. Solid symbols: the HM layers. Open symbols: the AP layers. The lines are power-law fits according to (1).

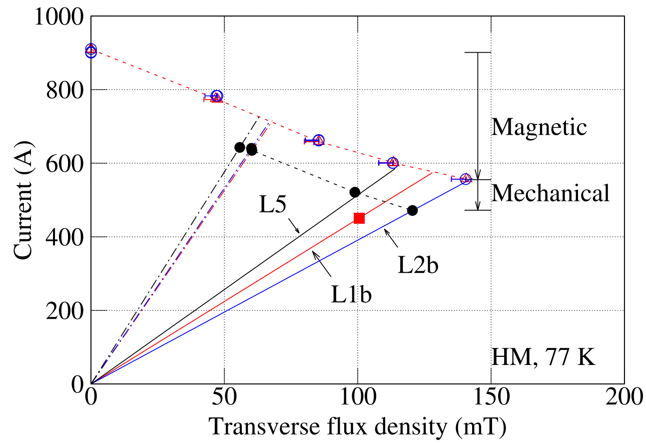

Fig. 14. Load lines of the conductor peak flux density for the HM layers. Red triangles and blue circles: the measured $I_c(B_{tra}, 77\text{ K})$ of the HM wires from Fig. 10. Dashed dotted lines: the conductor peak-field load lines before assembly. Solid lines: the conductor peak-field load lines after assembly. Black solid circles and red square: measured I_c of three HM layers. The vertical arrows illustrate the possible contribution to the current reduction in Layer 2b from the magnetic and mechanical factors.

TABLE V
I_c AND n-VALUE OF THE THREE HM LAYERS, BEFORE AND AFTER THE ASSEMBLY

Layer	77 K stand-alone		77 K assembled		4.2 K assembled	4.2 K/77 K
	I_c (A)	n (-)	I_c (A)	n (-)	I_c (A)	I_c ratio (-)
1b	635	24.2	450	5.9	$> 10,000$	> 22
2b	652	27.0	472	9.4	$> 10,000$	> 22
5	643	23.0	521	6.1	$> 10,000$	> 19

Fig. 13 shows the $V_2(I)$ across each layer of C3a at 77 K with a peak current of 518A. Three layers using the HM CORC wire showed a higher voltage than the other layers using with the AP wire.

Table V lists the I_c and n value of the HM wires in Layers 1b, 2b, and 5 at 77 K, before and after being assembled in the C3a magnet.

Fig. 14

shows the load lines of the conductor peak flux density for Layers 1b, 2b, and 5, stand-alone and after being assembled in the C3a magnet. Using the Biot–Savart law, we calculated the load lines of the peak flux density B_{tra} that is transverse to the longitudinal axis of the CORC wire (Appendix C). Layer 1b after assembly had a higher I_c reduction compared to the other two HM layers, which may indicate that Layer 1b suffered additional degradation during the magnet assembly.

Two factors can contribute to the current reduction in CORC wires at 77 K after winding into a coil.

First, a higher magnetic field on the wire. We quantified this effect by measuring the field dependence of the wire I_c at 77 K (Fig. 10 and Appendix C). The increased self-field on the wire led to about 20% reduction in the I_c of the HM wires in Layers 1b, 2b, and 5, higher than the 14% reduction in the AP wires in Layers 1 and 2 (Table IV). The stronger reduction was because the HM wires were more sensitive to the transverse field at 77 K (Fig. 10).

Second, excessive mechanical strain on REBCO tapes during coil fabrication. Mechanical strain can irreversibly degrade the wire I_c when the REBCO layer cracks. Assuming that the effects from the magnetic field and from the excessive mechanical strain simply added to the observed current decrease (Fig. 14), we concluded that the AP and HM wires, made in the 2021–2022 time frame, had similar bending performance. Both wires showed about 5% to 10% I_c degradation due to mechanical strain during the coil fabrication, at a minimum bend radius of 30 or 35 mm, with respect to the self-field I_c before magnet winding. In other words, we interpreted the difference between the expected self-field effect and the measured I_c as the winding degradation (Column "Difference" in Table IV). The retention

TABLE VI
EXPECTED SHORT-SAMPLE PREDICTION, I_{ssp}, AND THE CURRENT WHEN THE LAYER VOLTAGE INCREASED BY 2 μ V IN EACH LAYER DURING RAMP 17 AT 4.2 K BASED ON FIG. 17

Layer	Conductor	I_{ssp} (kA)	I at 2 μV (kA)	Ratio (-)
1b	HM	14.4	9.0	63%
2b	HM	13.8	9.0	65%
3	AP	9.5	5.7	60%
4	AP	9.3	5.2	56%
5	HM	15.4	8.0	52%
6	AP	10.8	4.8	44%

TABLE VII
PARTIAL TERMINATION RESISTANCE BASED ON $V_2(I)$ FOR EACH LAYER AT 77 AND 4.2 K

Layer	77 K Stand-alone (nΩ)	77 K Assembled (nΩ)	4.2 K Assembled (nΩ)
1b	0.9	52.4	1.5
2b	0.7	22.0	1.4
3	0.8	22.4	1.7
4	1.6	43.8	2.7
5	0.8	14.5	1.3
6	0.3	64.7	2.3

performance of the HM wires after bending was consistent with the findings at ACT [42].

Like the magnet development using strain-sensitive superconductors, mechanical strain effects in REBCO magnets are not unexpected and cannot be entirely prevented. The key is to control the amount of degradation due to strain by design and by manufacturing process controls.

Although both AP and HM wires showed a similar I_c retention after winding, the HM wires had a consistently higher n value than the AP wires (Table III). The n value for a CORC wire depends on several factors, such as the electrical termination resistance for each tape and the tape I_c [43], [44], [45], [46]. If the same termination fabrication procedure leads to a similar termination resistance for both AP and HM CCT layers, then a higher n value may indicate the REBCO tapes in the HM wires had a more similar I_c than those tapes in the AP wires.

The n value of the HM layers, however, decreased significantly from 25 before the magnet assembly to between 6 and 10 after the assembly (Table V). This can be related to the interfacing change between the termination and Cu adapter after the assembly. The decreased n value was indeed accompanied by the increased termination resistance (Table VII).

The increased transverse flux density on the wire reduced the n value too, but the n value remained above 15 (Fig. 11). Therefore, the increased field after winding alone cannot explain the reduction in n value. The change of the self-field distribution on the wire inside the termination, from a single-wire termination to a praying-hand joint of two wires, may have played a role.

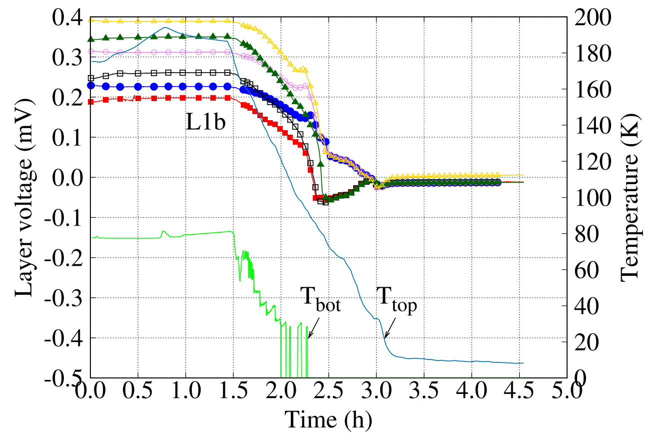

Fig. 15. Voltage across each layer of C3a at 100 mA during the cooldown to 4.2 K. The symbols are identical to those used in Fig. 12. Secondary y-axis: readings from the top and bottom temperature sensors.

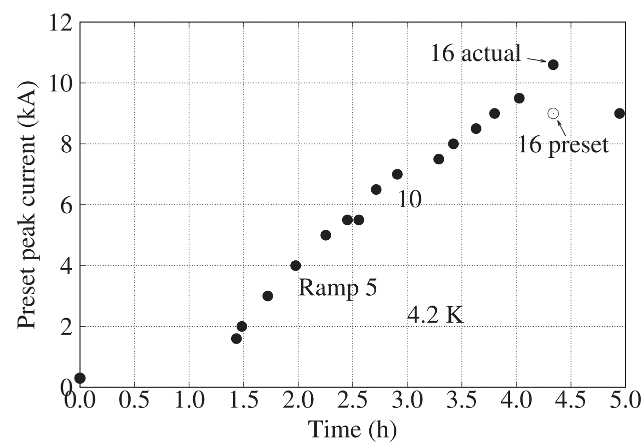

Fig. 16. Preset and actual peak current for each ramp at 4.2 K.

C. Magnet Behavior at 4.2 K

Fig. 15 shows the layer voltage during the cooldown to 4.2 K following the test in liquid nitrogen. The simultaneous superconducting transition (Figs. 12 and 15) was in strong contrast to the sequential transition of the layers in the C2 magnet where the layers were separated without fillers [31]. This indicated that the layers in the C3a magnet were better thermally coupled due to the Stycast between the layers.

We increased the peak current incrementally over the ramps as a primary and primitive way to avoid a thermal runaway. Fig. 16 shows the preset values of the peak current for a total of 17 ramps at 4.2 K.

Fig. 17 shows the $V_2(I)$ across each layer of C3a during Ramp 17. The current ramped at an averaged rate of 9.1 A s^{-1} from 500 to 9100 A and down to 50 A at the same rate. Three HM layers showed a lower voltage than the AP layers. Consistent with the tape performance (Fig. 2), the HM CORC wire carried less current at 77 K (Fig. 13) but more at 4.2 K.

Fig. 18 shows the load lines for the C3a magnet and the $I_c(B_{tra})$ of the HM and AP wires. The $I_c(B_{tra})$ data for the HM wire were extrapolated to lower fields from the data measured

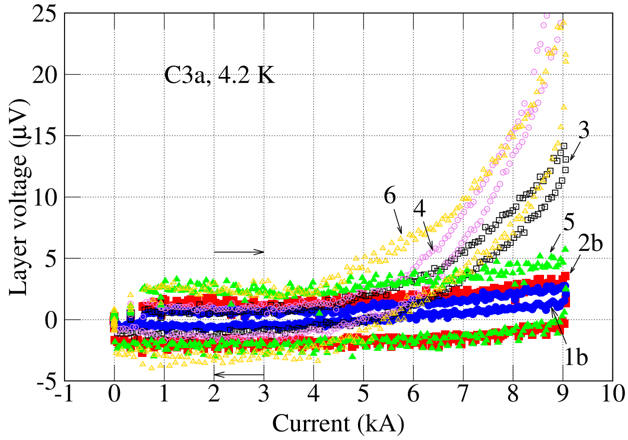

Fig. 17. $V_2(I)$ across each layer of the C3a magnet during Ramp 17. The labels indicate the layer number. Solid symbols: Layers 1b, 2b and 5 using the HM wire. Open symbols: Layers 3, 4 and 6 using the AP wire. The arrows indicate the up- and down-ramp branches.

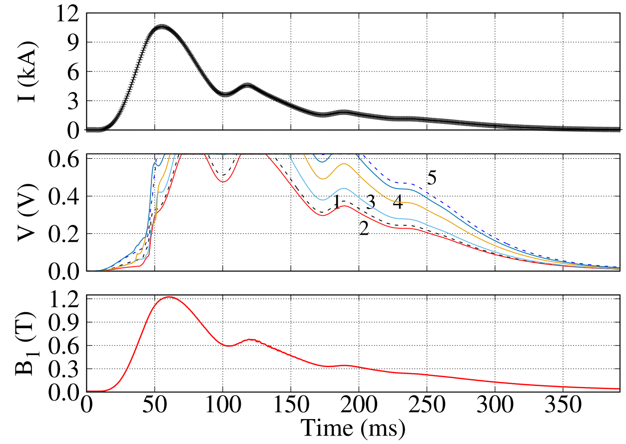

Fig. 19. Current transient, occurred at the end of Ramp 16 at 4.2 K, and the corresponding responses from the layer voltage and dipole field. The voltage data acquisition system cut off at about 0.6 V.

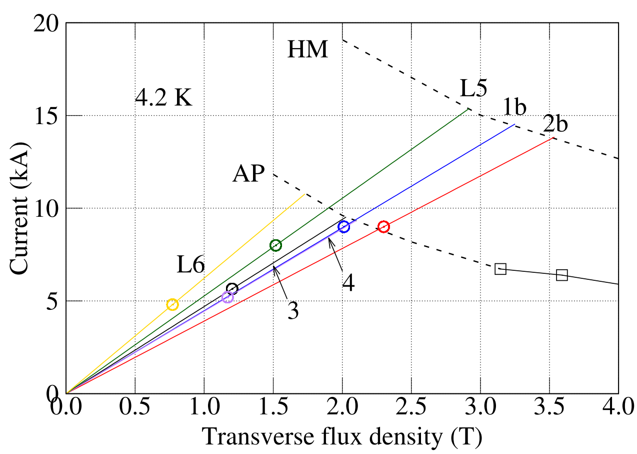

Fig. 18. Load lines for the C3a magnet at 4.2 K and the predicted performance. Dashed lines: the $I_c(B)$ for the HM and AP wires. Solid lines: the peak transverse field in each layer as a function of magnet current. Open circles: the current level where the layer voltage increased by 2 μV.

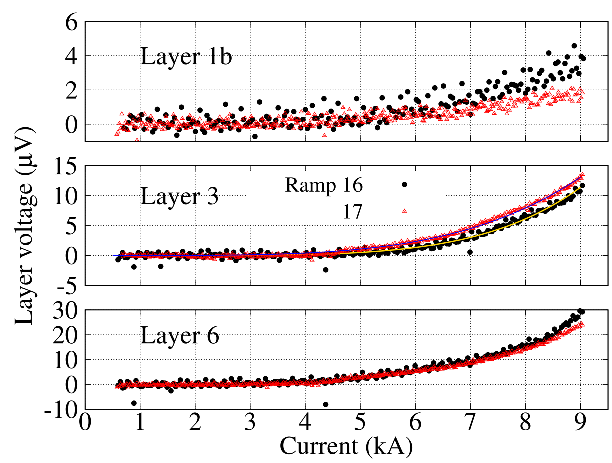

Fig. 20. $V(I)$ of Layers 1b, 3, and 6 before and after the current transient. Black solid circles: Ramp 16 before the transient. Red triangles: Ramp 17 after the transient.

on a prototype HM-CORC wire sample and scaled by a factor of 0.8 based on the I_c data of the REBCO tapes [42]. The $I_c(B_{tra})$ data from the C2 magnet were used for the AP wire.

Table VI gives the expected performance for each layer based on Fig. 18 and the measured current during Ramp 17 when the layer voltage increased by 2 μV from the up-ramp branch in Fig. 17.

The voltage across the AP layers started rising at around half of the short-sample prediction, indicating strong current sharing among the tapes inside the CORC wire and a high thermal stability of the REBCO conductor. A similar slow transition was also observed in a REBCO dipole magnet using Roebel cables [5] and a solenoid magnet using CORC wires [47]. Such a long transition over current can benefit the detection of the transition before the voltage runs away.

At 9.5 kA, the AP wires reached their full performance by obvious resistive transition while the HM wires showed less than 5 μV voltage rise. A similar HM CORC wire in background fields showed a voltage runaway at about 10 μV [42]. If the same behavior appears in a magnet using the HM wire, a fast and sensitive voltage comparison scheme will be needed to avoid the thermal runaway.

An unexpected transient current occurred at the end of Ramp 16 due to a power supply control issue. The current ramped from 50 A to 10.5 kA in about 50 ms, reaching an instantaneous ramp rate of 400 kA s^{-1} . Fig. 19 shows the measured magnet current, layer voltage, and dipole field during the transient. The dipole field increased at an averaged rate of about 20 T s^{-1}. The current transient also caused a significant and permanent shift in the fiber response [24].

After the unexpected transient, we had Ramp 17 with a ramp rate of 9.1 A s^{-1} between 50 and 9050A. We compared the $V(I)$ behaviors of each layer from Ramp 17 to those from the first part of Ramp 16 with a ramp rate of 41 A s^{-1} between 50 and 9050 A. Layers 1b and 6 showed a lower voltage during the transition after the transient (Fig. 20). Layers 2 and 5 showed a lower voltage too but less pronounced than Layers 1b and 6.

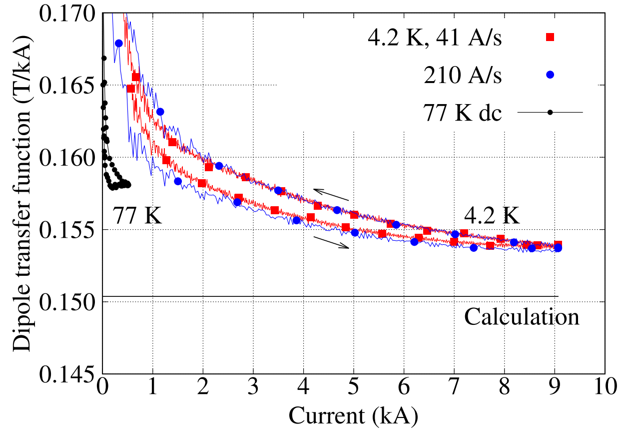

Fig. 21. Transfer function of the dipole field. Red squares: 41 A s^{-1} at 4.2 K. Blue circles: 210A s^{-1} at 4.2 K. Black circles: dc at 77 K. The arrows indicate the up- and down-ramp branches of the measured TF.

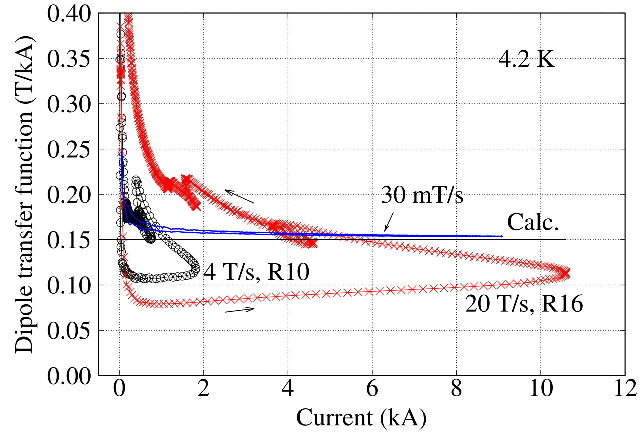

Fig. 22. Transfer function of the dipole field measured at different ramp rates at 4.2 K. Black open circles: 4 T s^{-1} . Red crosses: 20 T s^{-1}. Blue solid lines: 30 mT s^{-1} from Fig. 21. The arrows indicate the up- and down-ramp branches of the current.

The temperature of Layers 1b and 6 can be lower in Ramp 17 than in Ramp 16, leading to a lower voltages during the transition. Ramp 17 had a current ramp rate of 9.1 A s^{-1}, 22% of the rate in Ramp 16, which can lead to a lower temperature rise during the ramp. Ramp 16 started 12 min after Ramp 15 ended. Ramp 17 started 19 min after Ramp 16 ended. The longer interval can allow Layers 1b and 6 to recover to the bath temperature as they were close to the cryogen.

The I_c of Layer 3 reduced by 4% after the transient, from 8782 to 8448 A, based on a voltage criterion of 10 μV. The n value decreased from 5.3 to 4.2. Layer 4 showed no change. The current transient of 10.5 kA was 10% above the expected peak current for Layer 3 and 13% above that of Layer 4. The transient-induced heating likely degraded Layer 3. Considering the lower ramp rate in Ramp 17, Layer 4 likely also degraded, although much less pronounced than Layer 3.

D. Dipole Field At the Center of the Magnet Aperture

Fig. 21 shows the dipole transfer function at 77 and 4.2 K measured at the center of the magnet aperture. The measured transfer function is about 5% higher at 77 K and 3% higher at 4.2 K than the calculation. We ignored in the calculation the impact of 3% of iron in the mandrel that can increase the transfer function.

A current surge up to 2 kA preceded the normal ramp in most of the 17 tests at 4.2 K. Fig. 22 shows an example measured at a rate of about 37 kA s^{-1} or 4 T s^{-1} from Ramp 10. For comparison, we also included the data measured from Ramp 16 at 200 kA s^{-1} or 20 T s^{-1} and the data from a lower ramp rate at 210A s^{-1} or 30 mT s^{-1} from Fig. 21.

We attributed the strong hysteresis between the up and down branches to the eddy currents induced in the superconductor, metal mandrels and aluminum shell.

Fig. 23 shows that the dipole transfer function at the beginning of each current ramp changed as the peak magnet current of the previous ramp increased (Fig. 16).

The transfer function started from close to zero in Ramp 2 where the field penetration into the REBCO tape was minimal.

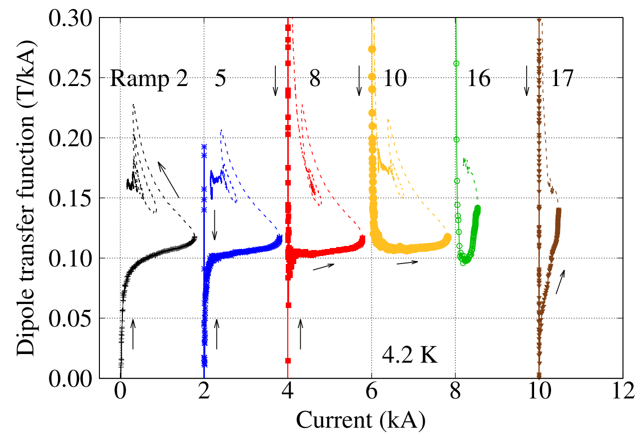

Fig. 23. Transfer function of the dipole field measured during the current surge from several tests. The curves are offset along the x-axis. Solid line points: the up ramp. Dashed lines: the down ramp.

The peak flux density on the REBCO tapes was lower than 70 mT at 300 A. As the magnet current increased and the magnetic field penetrated into REBCO conductor, the up-ramp branch of the transfer function changed the shape and became dominated by the remnant magnetization in the superconductors, as shown in Ramps 5, 8, and 10 in Fig. 23.

Temperature also affects the magnetization in the REBCO superconductor [48]. The transfer function of Ramp 17 was similar to Ramp 5 but differed from Ramp 16. We attributed it to a likely temperature rise in the conductor due to the transient current at the end of Ramp 16. The heating can be localized and the magnetization was not completely erased. Otherwise, the up-ramp branch of the measured transfer function would resemble that of Ramp 2. A similar behavior was observed in a recent measurement of REBCO solenoid coils [49].

E. Electrical Resistance of the Joints

The slope of the $V_2(I)$ data at current lower than 100 A corresponded to part of the termination resistance, as defined

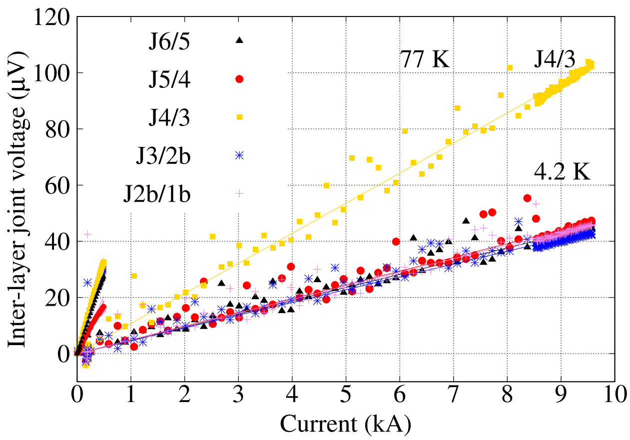

Fig. 24. Voltage across the inter-layer joints of C3a as a function of current at 77 and 4.2 K. The solid lines are the linear fit of the measured data.

TABLE VIII
RESISTANCE OF INTER-LAYER JOINTS AT 77 AND 4.2 K

Joint	V-tap group	77 K (nΩ)	4.2 K (nΩ)	Ratio (-)
6/5	D	57	4.7	12.1
5/4	C	38	4.9	7.7
4/3	D	69	10.7	6.4
3/2b	C	61	4.6	13.2
2b/1b	D	41	4.8	8.5

V-tap group from Fig. 8 is also included.

in (1). This partial termination resistance increased significantly after the assembly for each layer at 77 K and decreased at 4.2 K (Table VII).

The higher resistance was likely because the termination to Cu adapter interfacing changed after the assembly. When each layer was tested individually, current was transferred from the Cu adapter to the single termination. After the assembly, the current transferred from one termination to the other via the Cu adapter as the terminations were side by side in the interlayer joint. The change in the current-transfer path and length can affect the current distribution between the tapes and the termination resistance. It is unclear why the resistance significantly decreased at 4.2 K.

Fig. 24 shows the voltage across five praying-hand interlayer joints as a function of current at 77 and 4.2 K. The interlayer joint resistances decreased by a factor of 6 to 13 when the temperature was reduced from 77 to 4.2 K (Table VIII).

The electrical resistances of the terminations from the new indium-filling procedure were comparable to those in the C2 magnets at 77 and 4.2 K [31].

F. Deformation of the Wire Outside the Mandrel

After the test, we found that a few CORC wires deformed between the mandrel and the terminations (Fig. 25). A maximum deflection of about 1–2 mm occurred at the center of the 100-mm long wire segment.

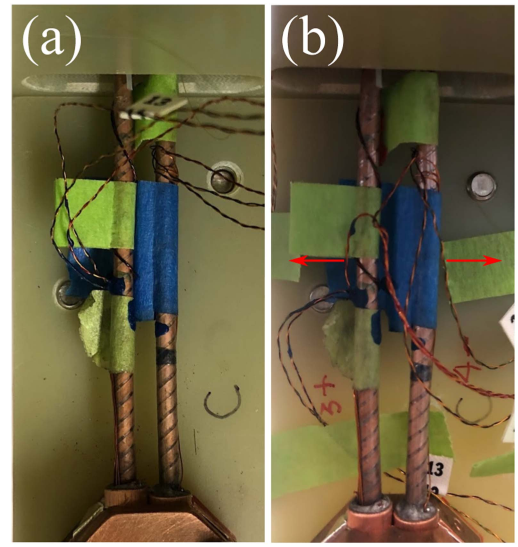

Fig. 25. Wires of Layers 3 and 4 at the return end. (a) Before the cold test. (b) After the test. The red arrows indicate the direction of the wire deformation.

Approximating the wires as line currents, we estimated the electromagnetic force on each wire to be 2.8 N mm^{-1} at 10.5 kA. Assuming the load was uniformly distributed on the 100-mm long round Cu core whose ends were fixed, we expect a maximum deflection of 3 mm at 10.5 kA, consistent with the observation (Fig. 25). The deformation might have contributed to the observed degradation in Layers 3 and 4 after the current transient, although Layer 6 deformed too but showed no obvious I_c degradation.

VI. CONCLUSION

In this article, we reported the fabrication and test of C3a, a six-layer subscale CCT dipole magnet. Three layers used the AP CORC wires and the other three used the HM wires. We addressed the following driving questions.

How to make and assemble the coils into a magnet?

1) Eight coils were wound using a semiautomated winding machine. An experienced human operator is still important. The operator attentively monitored the CORC wire when it entered the groove, especially in the pole region, nudging the wire into the groove when necessary. Nevertheless, using the new winder allowed a consistent and reproducible winding process for all the coils.
2) It is possible to automate the winding of CORC wires into a CCT dipole geometry with minimum hand touch. Winding the upcoming C3 magnet remains to be a critical test of the winder performance.
3) We filled the radial gaps between the layers using Stycast 2850 MT. The same process is feasible for the upcoming C3 magnet.

What is the bending and transport performance of the HM CORC wire?

1) The HM CORC wire carried a higher current than the AP wires at 4.2 K.

2) The AP and HM CORC wires, made in the 2021–2022 time frame, had similar bending performance. Both showed 5% to 10% I_c degradation due to mechanical strain during the coil fabrication, at a minimum bend radius of 30 or 35 mm, with respect to the self-field critical current before magnet winding.

What is the magnet performance?

1) At 77 K, the magnet reached a peak current of 518 A, limited by the HM layers, consistent with the lower I_c of the HM tapes at 77 K.
2) At 4.2 K, the magnet reached a peak current of 9.5 kA at a rate of 9.1 A s^{-1}, limited by the AP CORC wire, as expected from the estimated coil performance.
3) The voltage across each layer started rising at around half of the estimated short-sample prediction, indicating strong current sharing among the tapes inside the CORC wire and high thermal stability of the conductor.
4) After an unexpected current transient up to 10.5 kA over 50 ms, the I_c of Layer 3 decreased by 4% based on a voltage criterion of 10 μV.
5) A strong hysteresis of the dipole field transfer function was observed when the ramp rate was on the order of 10 T s^{-1} . At 6 kA, the up-ramp branch of the transfer function reduced by 40% from 0.155 T kA^{-1} at 30 mT s^{-1} to 0.093 T kA^{-1} at 20 T s^{-1}.
6) The dipole field was affected by the magnetization in REBCO conductors and a potential temperature rise in the coil due to the current transient.

What is the performance of the electrical joints? The new procedure to fill molten indium in the termination worked. The resistance of the interlayer joints ranged from 5–11 nΩ at 9.5 kA, comparable to the performance of the earlier terminations. We expect the new termination to work for the upcoming C3 magnet.

The exercise of the C3a magnet also helped identified several issues to be addressed for the upcoming C3 magnet.

1) The long straight layout of the CORC wire required additional handling during coil winding that can risk degrading the conductor. It is desirable to avoid such a layout.
2) The voltage-tap wire should follow the CORC wire to minimize the inductive voltage during current ramping.
3) Support the CORC wires between the mandrel and termination adapters against the electromagnetic forces.
4) Prepare to keep the layer voltage low, such as below 10 μV, to avoid thermal runaway.
5) Unexpected current transient needs to be avoided.

There will be unknowns and issues for the upcoming C3 magnet. The exercise and results from the subscale C3a magnet prepared us to address them.

Appendix A
Fill the Layer Gaps Using Stycast

To determine the minimum radial clearance that Stycast 2850MT can flow, we inserted a 1-m-long aluminum cylinder into a clear acrylic tube of the same length and injected the Stycast into the radial gap. After the Stycast cured, we cut a section of the cylinder where the Stycast only partially filled the radial gap due to the varying clearance along the circumference of the cylinder. By measuring the thickness of the cured Stycast layer that was retrieved from the section, we determined that the alumina-filled Stycast 2850 MT can flow through a minimum radial clearance of 250 μm.

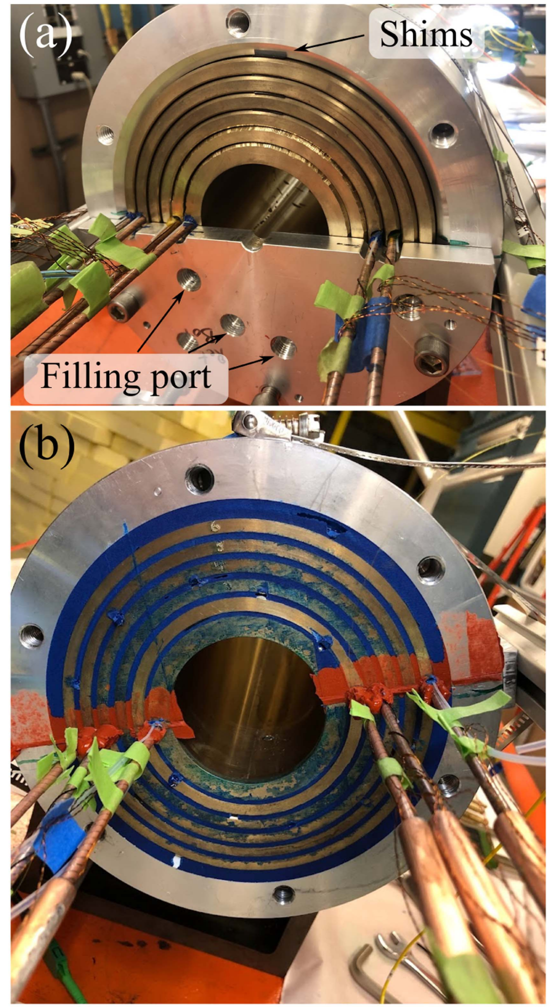

Fig. 26. (a) Before filling the radial gaps with the epoxy, viewed from the return end of the magnet. The bottom half of the aluminum plate is installed. (b) After filling the Stycast. The red sealant can be seen.

We practiced the following setup and procedure of Stycast filling. The magnet was horizontal during the filling process.

We first sealed both ends of the magnet using aluminum plates. The plates were two halves and were assembled from the sides to clear for the CORC wires and other instrumentation wiring. Several ports were machined on the plates to allow the epoxy injection at the lead end and release at the return end [Fig. 26(a)]. The ports were aligned with the radial gaps. Two ports were available for each radial gap.

The aluminum plates were pressed against the end surfaces of the layers to prevent the epoxy from flowing between the gaps. We applied masking tapes to the surface of the plates at the lead end to compensate for the slightly different lengths of the mandrels which were aligned at the return end. The gap between the two half plates was sealed using a silicone sealant [DAP High Temp 100% RTV, Fig. 26(b)].

Before filling epoxy, we did a pressure test on each radial gap by injecting compressed air through the associated filling port. The pressure reached 24 kPa when the system started leaking. The pressure decreased to 6.9 kPa within 3 s after removing the compressed air.

When filling one radial gap, we sealed the injection and exhausting tubes for the other radial gaps to help guide the epoxy into the desired radial gap. We injected the epoxy, with a maximum pressure of 138 kPa, into both ports for a radial gap until it appeared in the exhaust tubes at the return end. We then sealed the exhausting tubes and continued pressurizing the dispenser. If the pressure held, we sealed the injection tubes and started filling the next radial gap. It took about 20 min to fill one radial gap. Fig. 26(b) shows the return-end surface after the epoxy cured. The process went well with only a minor overflow from the radial gap between Layers 3 and 4.

We do not know, however, if the Stycast completely filled each radial gap, even though the amount of the Stycast used for the filling process was 20% to 25% higher than the expected value based on the clearance volume between the concentric cylinders. Two indications suggested that the gaps should be filled. First, the simultaneous superconducting transition of all six layers during the cooldown (Figs. 12 and 15) suggested a good thermal coupling between the layers through Stycast. Second, the deformation of the aluminum shell, as measured by the optical fiber [24], also supported that the layers were mechanically coupled through the Stycast.

Appendix B
Measure the Critical Current of CORC Wires as a Function of Applied Magnetic Field at 77 K

We cut the CORC wire to length and measured the I_c before winding. The wire was bent to a "U" shape with a bend radius of around 190 mm to have a self-field similar to that of a straight wire (Fig. 27).

The applied magnetic field, transverse to the longitudinal axis of the wire, was generated by a split-pair copper electromagnet (Magnetech Corporation R-5030-24). There was a nominal gap of 12.7 mm between the pole surfaces of the magnets (Fig. 27).

When submerged in liquid nitrogen at 77 K, the electromagnet can generate a steady-state magnetic field of up to 0.5 T over a 50-mm long conductor segment based on the field profile measured at room temperature (Fig. 28).

The CORC wire was sandwiched between two G10 boards, each 6.35-mm thick, to minimize the lateral displacement of the wire under the electromagnetic force. A calibrated cryogenic Hall sensor (Lakeshore HGCT 3020) was mounted below the wire to measure the flux density between the poles.

We started the test by measuring the I_c of the CORC wire in self-field. After the electromagnet was turned on, we waited for 20 s to stabilize the applied magnetic field before injecting current into the CORC wire. We reported the stable flux density before injecting the current as the applied flux density for each $V(I)$ measurement. After a series of in-field $V(I)$ measurements, the test ended with another self-field measurement to verify that the conductor did not degrade.

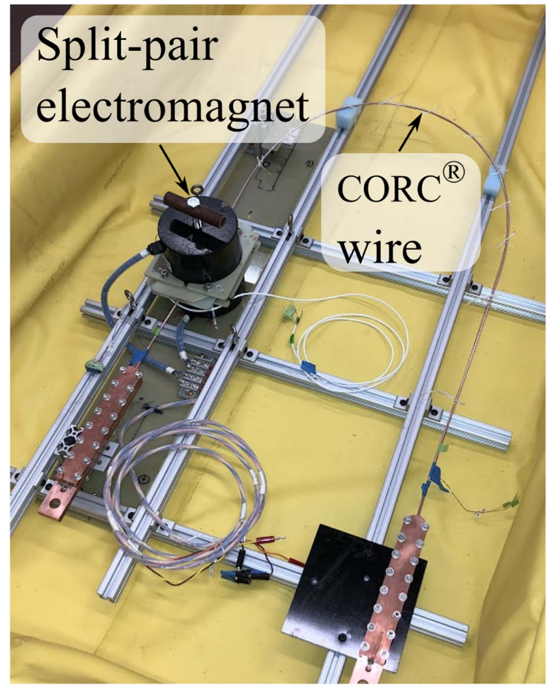

Fig. 27. Setup to measure the critical current of a CORC wire before winding as a function of applied transverse flux density.

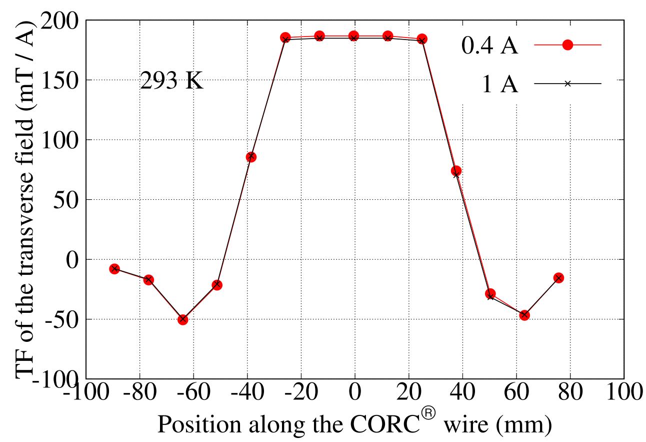

Fig. 28. Transfer function of the magnetic field transverse to the pole surface of the split-pair electromagnet, measured at room temperature.

Appendix C
Expected Coil Performance at 77 K

Comparing the measured and expected coil performance at 77 K can provide an early and cost-effective way to evaluate the coil fabrication and conductor performance.

We assume that the maximum current that a CORC coil can carry at certain voltage criterion is determined by the flux density that is transverse to the longitudinal central axis of the CORC wire. Suppose the flux density is $\mathbf{B}$ at Point P on the longitudinal axis of a CORC wire. We decompose $\mathbf{B}$ into two orthogonal vectors: 1) $\mathbf{B}_{\tan}$ that is tangent to the wire axis; and 2) $\mathbf{B}_{\rm tra}$ that is transverse to the wire axis (Fig. 29).

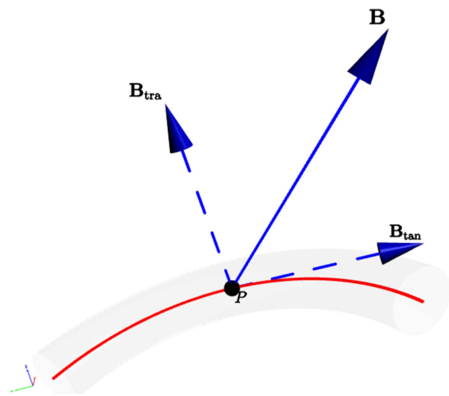

Fig. 29. Flux density $\mathbf{B}$ at Point P on the longitudinal axis of a CORC wire. The red line represents the longitudinal axis of the wire. $\mathbf{B}$ is decomposed into two orthogonal components, one tangent and the other transverse to the longitudinal axis.

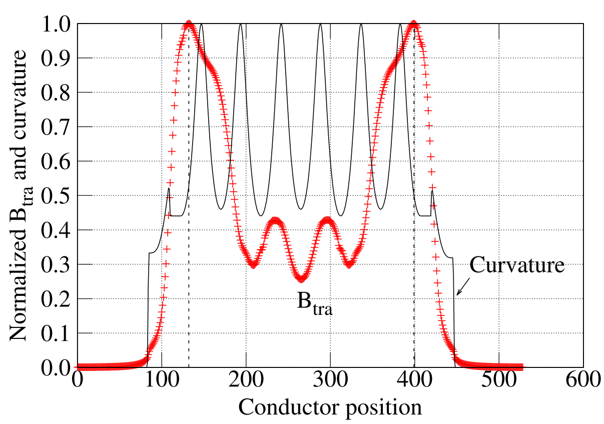

Fig. 30. B_{tra}, symbols, and curvature, black solid line, along the CORC wire for C3a Layer 1. The data are determined every 3-mm along the longitudinal axis of the CORC wire. Both B_{tra} and curvature are normalized to their respective peak values. The dashed lines show the location of the peak B_{tra} and corresponding curvature of the wire.

The transverse component is given by

$$\mathbf{B}_{\mathrm{tra}} = \mathbf{B} - \mathbf{B}_{\tan} \tag{2}$$

where $\mathbf{B}_{\tan} = \mathbf{B} \cdot \mathbf{t}$ and $\mathbf{t}$ is the unit tangent vector of the conductor longitudinal axis at P. $\mathbf{t}$ can be analytically determined for a CCT winding path. $\mathbf{B}$ is calculated according to the Biot–Savart law given the conductor layout in a coil.

The intersection of two curves, the calculated $B_{\mathrm{tra}}(I)$ and measured $I_{\mathrm{c}}(B_{\mathrm{tra}})$, gives the expected coil performance at 77 K. The results are given by Column "Self-field effect only" in Table IV.

The peak B_{tra} in each individual layer, stand-alone or in the C3a magnet, is located near the midplane region. As an example, Fig. 30 shows the local B_{tra} and curvature of the wire normalized to their peak values for Layer 1. At the peak B_{tra} location, the CORC wire has a bend radius of 60 mm. B_{tra} reduces to about 92% of the peak B_{tra} value at the first and last poles where the minimum bend radius is 30 mm.

Since the peak B_{tra} is located near the midplane region where the local bend radius is more than 60 mm, we consider the $I_{\mathrm{c}}(B)$ data measured from a straight CORC wire relevant to determine the expected performance for the C3a coils at 77 K.

Appendix D
Timelines of the C3a Development

The design of the C3a started in January 2020. We started making Layer 1 in July 2022 and completed the last layer in May 2023. The C3a magnet was assembled during the summer of 2023, followed by the tests at 77 and 4.2 K in November 2023.

A 26-m long AP CORC wire was ordered in July and October 2021 and was delivered in December 2021. The HM tapes became sufficiently available to make prototype CORC wires in July 2022. We ordered a 10-m long HM CORC wire that was delivered in November 2022.

The development of Winder Mark 2 started in April 2019. The first winding test using a Cu dummy wire took place in November 2020, followed by the winding of a subscale CCT magnet using STAR wires [17]. We wound eight three-turn coils for the C3a magnet using the winder between July 2022 and April 2023. A[2] youtube video shows the winding of Layer 3 as an example.

Acknowledgment

The authors would like to thank Toru Fukushima, Tetsu Tateishi, Yifei Zhang and Drew Hazelton of SuperPower Inc. for leading the production of HM REBCO tapes used here. The authors would also like to thank Bun Pa Lim and Kristopher Pearson at the LBNL main shop for making the mandrels, Matthew Reynolds for installing the strain gauges and optical fiber, Timothy Bogdanof and Maxwell Maruszewski for helping with the Stycast filling test, and Michael Naus for arranging the liquid helium order and delivery. The authors would like to thank Derek Hochvert, Simone Johnson, and Robert Memmo for their support on the coil fabrication and magnet test. The authors would also like to thank David Larbalestier, Van Griffin, James Maddox, and James Gilman of National High Magnetic Field Laboratory for providing the test cryostat. William B. Ghiorso developed the original concept and design of Winder Mark 2. Hugh Higley provided vital feedback and validation. Tom Lipton supplied critical mechanism design details. Hugh Higley developed the technique and procedure to make the flute-type electrical termination. Conductor used in this work was procured by U.S. MDP, Conductor Procurement and R&D, supported by the Office of High Energy Physics, U. S. Department of Energy.

References

[1] W. Barletta et al., "Future hadron colliders: From physics perspectives to technology R&D," *Nucl. Instruments Methods Phys. Res. Sect. A., Accelerators, Spectrometers, Detectors Assoc. Equip.*, vol. 764, pp. 352–368, Nov. 2014.

[2] S. A. Gourlay, "Superconducting accelerator magnet technology in the 21st century: A new paradigm on the horizon?," *Nucl. Instruments Methods Phys. Res. A*, vol. 893, pp. 124–137, Jun. 2018.

[3] G. Sabbi, "High-field magnets for future hadron colliders," *Annu. Rev. Nucl. Part. Sci.*, vol. 74, no. 1, pp. 389–415, Sep. 2024.

[4] M. Durante et al., "Realization and first test results of the EuCARD 5.4-T REBCO dipole magnet," *IEEE Trans. Appl. Supercond.*, vol. 28, no. 3, Apr. 2018, Art. no. 4203805.

[2][Online]. Available: https://youtu.be/RReYmc_1rCs

[5] J. van Nugteren et al., "Powering of an HTS dipole insert-magnet operated standalone in helium gas between 5 and 85 K," *Superconductor Sci. Technol.*, vol. 31, no. 6, Apr. 2018, Art. no. 065002.
[6] L. Rossi and C. Senatore, "HTS accelerator magnet and conductor development in Europe," *Instruments*, vol. 5, no. 1, Feb. 2021, Art. no. 8.
[7] S. A. Gourlay et al., "The U.S. magnet development program plan," U.S. Dept. Energy, Washington, DC, USA, Jun. 2016. [Online]. Available: https://escholarship.org/uc/item/5178744r
[8] S. Prestemon et al., "The 2020 updated roadmaps for the US magnet development program," Oct. 2020, *arXiv:2011.09539*. [Online]. Available: http://arxiv.org/abs/2011.09539
[9] D. C. van der Laan, "$YBa_2Cu_3O_{7-\delta}$ coated conductor cabling for low ac-loss and high-field magnet applications," *Superconductor Sci. Technol.*, vol. 22, no. 6, 2009, Art. no. 065013.
[10] J. D. Weiss et al., "Introduction of CORC wires: Highly flexible, round high-temperature superconducting wires for magnet and power transmission applications," *Superconductor Sci. Technol.*, vol. 30, no. 1, 2017, Art. no. 014002.
[11] D. C. van der Laan, J. D. Weiss, and D. M. McRae, "Status of CORC cables and wires for use in high-field magnets and power systems a decade after their introduction," *Superconductor Sci. Technol.*, vol. 32, no. 3, Feb. 2019, Art. no. 033001.
[12] W. Luo et al., "Superior critical current of symmetric tape round (STAR) REBCO wires in ultra-high background fields up to 31.2 T," *Superconductor Sci. Technol.*, vol. 31, no. 12, Nov. 2018, Art. no. 12LT01.
[13] S. Kar et al., "Symmetric tape round REBCO wire with J_e (4.2 K, 15 T) beyond 450 A mm^{-2} at 15 mm bend radius: A viable candidate for future compact accelerator magnet applications," *Superconductor Sci. Technol.*, vol. 31, no. 4, Mar. 2018, Art. no. 04LT01.
[14] V. V. Kashikhin et al., "Accelerator magnet development based on COMB technology with STAR wires," *IOP Conf. Series. Materials Sci. Eng.*, vol. 1301, no. 1, May 2024, Art. no. 012153.
[15] R. Gupta et al., "New approach and test facility for high-field accelerator magnets R&D," *IEEE Trans. Appl. Supercond.*, vol. 30, no. 4, Jun. 2020, Art. no. 4000106.
[16] X. Wang et al., "A viable dipole magnet concept with REBCO CORC wires and further development needs for high-field magnet applications," *Superconductor Sci. Technol.*, vol. 31, no. 4, Mar. 2018, Art. no. 045007.
[17] X. Wang et al., "An initial magnet experiment using high-temperature superconducting STAR wires," *Superconductor Sci. Technol.*, vol. 35, no. 12, Nov. 2022, Art. no. 125011.
[18] J. L. Rudeiros Fernández and P. Ferracin, "Uni-layer magnets: A new concept for LTS and HTS based superconducting magnets," *Superconductor Sci. Technol.*, vol. 36, no. 5, Mar. 2023, Art. no. 055003.
[19] H. G. Khodzhibagiyan et al., "Quadrupole superconducting model magnet for upgrade of the nuclotron synchrotron," *IEEE Trans. Appl. Supercond.*, vol. 32, no. 6, Sep. 2022, Art. no. 4003704.
[20] N. Amemiya et al., "Effective reduction of magnetisation losses in copper-plated multifilament coated conductors using spiral geometry," *Superconductor Sci. Technol.*, vol. 35, no. 2, Feb. 2022, Art. no. 025003.
[21] N. Amemiya et al., "Measurements of coupling time constants and geometry factors of coupling losses in spiral copper-plated multifilament coated conductors," *IEEE Trans. Appl. Supercond.*, vol. 32, no. 6, Sep. 2022, Art. no. 6602005.
[22] N. Amemiya et al., "Progress of fabrication and characterizations of SCSC cables toward winding coils," presented at the 2024 Appl. Supercond. Conf., Salt Lake City, UT, USA, Sep. 1–6, 2024.
[23] L. Fan et al., "Design and testing of a prototype canted-cosine-theta HTS dipole magnet using CORC cable," *IEEE Trans. Appl. Supercond.*, vol. 34, no. 3, May 2024, Art. no. 4600605.
[24] L. Luo et al., "Distributed fiber-optic sensing in a subscale high-temperature superconducting dipole magnet," *Superconductor Sci. Technol.*, vol. 38, no. 3, Mar. 2025, Art. no. 035029.
[25] SuperPower Inc., Glenville, NY, USA, "2G HTS wire specification," Accessed: Jan. 14 2024. [Online]. Available: https://www.superpower-inc.com/specification.aspx
[26] D. Abraimov et al., "Double disordered YBCO coated conductors of industrial scale: High currents in high magnetic field," *Superconductor Sci. Technol.*, vol. 28, no. 11, Nov. 2015, Art. no. 114007.
[27] A. Francis et al., "Development of general expressions for the temperature and magnetic field dependence of the critical current density in coated conductors with variable properties," *Superconductor Sci. Technol.*, vol. 33, no. 4, Feb. 2020, Art. no. 044011.
[28] A. Godeke et al., "Bi-2212 canted-cosine-theta coils for high-field accelerator magnets," *IEEE Trans. Appl. Supercond.*, vol. 25, no. 3, Jun. 2015, Art. no. 4002404.
[29] D. Arbelaez et al., "Status of the Nb_3Sn canted-cosine-theta dipole magnet program at Lawrence Berkeley national laboratory," *IEEE Trans. Appl. Supercond.*, vol. 32, no. 6, Sep. 2022, Art. no. 4003207.
[30] T. Shen et al., "Design, fabrication, and characterization of a high-field high-temperature superconducting Bi-2212 accelerator dipole magnet," *Phys. Rev. Accelerators Beams*, vol. 25, no. 12, Dec. 2022, Art. no. 122401.
[31] X. Wang et al., "Development and performance of a 2.9 Tesla dipole magnet using high-temperature superconducting CORC wires," *Superconductor. Sci. Technol.*, vol. 34, no. 1, Dec. 2020, Art. no. 015012.
[32] L. N. Brouwer, "Canted-cosine-theta superconducting accelerator magnets for high energy physics and ion beam cancer therapy," Ph.D. dissertation, Univ. California, Berkeley, Berkeley, CA, USA, 2015, [Online]. Available: https://escholarship.org/uc/item/8jp4g75g
[33] D. van der Laan, "Superconducting cable connections and methods," US Patent 9, 755,329, 9 2017.
[34] T. Mulder et al., "Optimized and practical electrical joints for CORC type HTS cables," in *Proc. Materials Sci. Eng. Conf. Ser.*, Dec. 2015, vol. 102, Art. no. 012026.
[35] N. Castaneda et al., "A 6-around-1 cable using high-temperature superconducting STAR wires for magnet applications," *Superconductor Sci. Technol.*, vol. 37, no. 3, Mar. 2024, Art. no. 035009.
[36] S. Caspi, "A video from Glyn Kirby on an automated winding table developed at CERN for a CCT magnet," private communication, Sep. 16, 2018.
[37] N. Amemiya et al., "Progress of research and development of fundamental technologies for accelerator magnets using coated conductors," *IEEE Trans. Appl. Supercond.*, vol. 23, no. 3, Jun. 2013, Art. no. 4601905.
[38] H. Reymond et al., *Development of an Automated High Temperature Superconductor Coil Winding Machine at CERN*. Geneva, Switzerland: JACoW Publishing, Mar. 2022.
[39] M. Marchevsky and S. Prestemon, "Distributed thermometry for superconducting magnets using non-leaky acoustic waveguides," *Superconductor Sci. Technol.*, vol. 36, no. 4, Apr. 2023, Art. no. 045005.
[40] J. Fleiter, A. Bonasia, and A. Ballarino, "Rutherford cable production report Nb-Ti cable H17BC0264A02 (MQXF lead)," CERN, Geneva, Switzerland, Tech. Rep., 2018.
[41] L. Bottura, "A practical fit for the critical surface of NbTi," *IEEE Trans. Appl. Supercond.*, vol. 10, no. 1, pp. 1054–1057, Mar. 2000.
[42] D. C. van der Laan et al., "CORC wires allowing bending to 20 mm radius with 97.5 % retention in critical current and having an engineering current density of 530 A/mm^2 at 20 T," *Superconductor Sci. Technol.*, vol. 37, no. 11, 2024, Art. no. 115007 .
[43] G. P. Willering et al., "Effect of variations in terminal contact resistances on the current distribution in high-temperature superconducting cables," *Superconductor Sci. Technol.*, vol. 28, no. 3, Jan. 2015, Art. no. 035001.
[44] M. Takayasu, L. Chiesa, N. C. Allen, and J. V. Minervini, "Present status and recent developments of the twisted stacked-tape cable conductor," *IEEE Trans. Appl. Supercond.*, vol. 26, no. 2, Mar. 2016, Art. no. 6400210.
[45] A. C. Araujo Martínez, Q. Ji, S. O. Prestemon, X. Wang, and G. H. I. Maury Cuna, "An electric-circuit model on the inter-tape contact resistance and current sharing for REBCO cable and magnet applications," *IEEE Trans. Appl. Supercond.*, vol. 30, no. 4, Jun. 2020, Art. no. 6600605.
[46] R. Teyber et al., "Numerical investigation of current distributions around defects in high temperature superconducting CORC cables," *Superconductor Sci. Technol.*, Aug., vol. 35, no. 9, 2022, Art. no. 094008.
[47] D. C. Van Der Laan et al., "A CORC cable insert solenoid: The first high-temperature superconducting insert magnet tested at currents exceeding 4 kA in 14 T background magnetic field," *Superconductor Sci. Technol.*, vol. 33, no. 5, Apr. 2020, Art. no. 05LT03.
[48] K.-H. Mess, P. Schmüser, and S. Wolff, *Superconducting Accelerator Magnets*. Singapore: World Scientific, 1996, ch. 6.
[49] A. Zampa et al., "Screening and coupling currents induced fields on a large-scale prototype REBCO insulated coil," *IEEE Trans. Appl. Supercond.*, vol. 34, no. 5, Aug. 2024, Art. no. 4700205.